












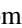




















# The Core Mass Function in the Orion Nebula Cluster Region: What Determines the Final Stellar Masses?

Hideaki Takemura<sup>1,2</sup> , Fumitaka Nakamura<sup>1,2,3</sup> , Shuo Kong<sup>4,5</sup> , Héctor G. Arce<sup>5</sup> , John M. Carpenter<sup>6</sup> ,  
Volker Ossenkopf-Okada<sup>7</sup> , Ralf Klessen<sup>8,9</sup> , Patricio Sanhueza<sup>1,2</sup> , Yoshito Shimajiri<sup>2</sup> , Takashi Tsukagoshi<sup>2</sup> ,  
Ryohei Kawabe<sup>1,2</sup> , Shun Ishii<sup>2</sup> , Kazuhito Dobashi<sup>10</sup> , Tomomi Shimoikura<sup>11</sup> , Paul F. Goldsmith<sup>12</sup> ,  
Álvaro Sánchez-Monge<sup>7</sup> , Jens Kauffmann<sup>13</sup> , Thushara G. S. Pillai<sup>14</sup> , Paolo Padoan<sup>15,16</sup> , Adam Ginsberg<sup>17</sup> ,  
Rowan J. Smith<sup>18</sup> , John Bally<sup>19</sup> , Steve Mairs<sup>20</sup> , Jaime E. Pineda<sup>21</sup> , Dariusz C. Lis<sup>12</sup> , Blakesley Burkhart<sup>22</sup> ,  
Peter Schilke<sup>7</sup> , Hope How-Huan Chen<sup>23</sup> , Andrea Isella<sup>24</sup> , Rachel K. Friesen<sup>25</sup>, Alyssa A. Goodman<sup>26</sup> , and  
Doyal A. Harper<sup>27</sup>

<sup>1</sup> The Graduate University for Advanced Studies (SOKENDAI), 2-21-1 Osawa, Mitaka, Tokyo 181-0015, Japan

<sup>2</sup> National Astronomical Observatory of Japan, 2-21-1 Osawa, Mitaka, Tokyo 181-8588, Japan

<sup>3</sup> Department of Astronomy, The University of Tokyo, Hongo, Tokyo 113-0033, Japan

<sup>4</sup> Steward Observatory, University of Arizona, Tucson, AZ 85719, USA

<sup>5</sup> Department of Astronomy, Yale University, New Haven, CT 06511, USA

<sup>6</sup> Joint ALMA Observatory, Alonso de Córdova 3107 Vitacura, Santiago, Chile

<sup>7</sup> I. Physikalisches Institut, Universität zu Köln, Zùlpicher Str. 77, D-50937 Köln, Germany

<sup>8</sup> Universität Heidelberg, Zentrum für Astronomie, Albert-Ueberle-Str. 2, D-69120 Heidelberg, Germany

<sup>9</sup> Universität Heidelberg, Interdisziplinäres Zentrum für Wissenschaftliches Rechnen, INF 205, D-69120 Heidelberg, Germany

<sup>10</sup> Tokyo Gakugei University, Koganei, Tokyo, 184-8501, Japan

<sup>11</sup> Otsuma Women's University, Chiyoda-ku, Tokyo, 102-8357, Japan

<sup>12</sup> Jet Propulsion Laboratory, California Institute of Technology, 4800 Oak Grove Drive, Pasadena, CA 91109, USA

<sup>13</sup> Haystack Observatory, Massachusetts Institute of Technology, 99 Millstone Road, Westford, MA 01886, USA

<sup>14</sup> Institute for Astrophysical Research, Boston University, 725 Commonwealth Avenue, Boston, MA 02215, USA

<sup>15</sup> Institut de Ciències del Cosmos, Universitat de Barcelona, IEEC-UB, Martí i Franqués 1, E-08028 Barcelona, Spain

<sup>16</sup> ICREA, Pg. Lluís Companys 23, E-08010 Barcelona, Spain

<sup>17</sup> Department of Astronomy, University of Florida, Gainesville, FL 32611, USA

<sup>18</sup> Jodrell Bank Centre for Astrophysics, School of Physics and Astronomy, University of Manchester, Oxford Road, Manchester M13 9PL, UK

<sup>19</sup> Department of Astrophysical and Planetary Sciences, University of Colorado, Boulder, CO, USA

<sup>20</sup> East Asian Observatory, 660 N. A'ohökü Place, Hilo, HI 96720, USA

<sup>21</sup> Max-Planck-Institut für extraterrestrische Physik, Giessenbachstrasse 1, D-85748 Garching, Germany

<sup>22</sup> Department of Physics and Astronomy, Rutgers, The State University of New Jersey, 136 Frelinghuysen Road, Piscataway, NJ 08854, USA

<sup>23</sup> Department of Astronomy, The University of Texas, Austin, TX 78712, USA

<sup>24</sup> Department of Physics and Astronomy, Rice University, 6100 Main Street, Houston, TX 77005, USA

<sup>25</sup> National Radio Astronomy Observatory, 520 Edgemont Road, Charlottesville, VA 22903, USA

<sup>26</sup> Harvard-Smithsonian Center for Astrophysics, 60 Garden Street, MS 42, Cambridge, MA 02138, USA

<sup>27</sup> Department of Astronomy and Astrophysics University of Chicago, Chicago, IL 60637, USA

Received 2020 October 8; revised 2021 February 8; accepted 2021 February 9; published 2021 March 22

## Abstract

Applying dendrogram analysis to the CARMA-NRO C<sup>18</sup>O ( $J = 1-0$ ) data having an angular resolution of  $\sim 8''$ , we identified 692 dense cores in the Orion Nebula Cluster region. Using this core sample, we compare the core and initial stellar mass functions in the same area to quantify the step from cores to stars. About 22% of the identified cores are gravitationally bound. The derived core mass function (CMF) for starless cores has a slope similar to Salpeter's stellar initial mass function (IMF) for the mass range above  $1 M_{\odot}$ , consistent with previous studies. Our CMF has a peak at a subsolar mass of  $\sim 0.1 M_{\odot}$ , which is comparable to the peak mass of the IMF derived in the same area. We also find that the current star formation rate is consistent with the picture in which stars are born only from self-gravitating starless cores. However, the cores must gain additional gas from the surroundings to reproduce the current IMF (e.g., its slope and peak mass), because the core mass cannot be accreted onto the star with 100% efficiency. Thus, the mass accretion from the surroundings may play a crucial role in determining the final stellar masses of stars.

*Unified Astronomy Thesaurus concepts:* [Star formation \(1569\)](#); [Interstellar medium \(847\)](#); [Molecular clouds \(1072\)](#); [Protostars \(1302\)](#); [Radio observatories \(1350\)](#); [CO line emission \(262\)](#); [Initial mass function \(796\)](#)

## 1. Introduction

Stars are believed to form in the dense parts of molecular clouds, called dense cores (e.g., Shu et al. 1987). However, the evolution of such cores, particularly the process of star formation, is a matter of debate. There are two scenarios widely discussed so far: competitive accretion (Bonnell & Bate 2006) and core-collapse models (e.g., Shu et al. 1987; McKee & Tan 2003). In the competitive accretion scenario, stellar seeds,

which are formed from the local dense parts of the core, initially have low masses of  $\sim 1 M_{\odot}$ , and gain additional mass from the surroundings through the modified Bondi–Hoyle accretion. The mass function of dense cores (CMF) of the stellar seeds is likely to be different in shape from the stellar initial mass function (IMF) at least at the early evolutionary phase (e.g., Zinnecker 1982; Goodwin et al. 2008). In the core-collapse model, final stellar masses are largely determined by the masses of the

progenitor cores. Thus, a one-to-one correspondence between the core mass and stars formed is likely to be a natural outcome. A hybrid model, the clump-fed model, has also been proposed (Wang et al. 2010), where massive cores preferentially located at the bottom of the gravitational potential tend to gain additional mass through accretion of ambient gas. The converging flow and global gravitational collapse scenarios have also been widely discussed and attempt to explain observational characteristics of star-forming regions (Klessen et al. 1998; Klessen & Hennebelle 2010; Vázquez-Semadeni et al. 2019; Ballesteros-Paredes et al. 2020). Recent numerical simulations have pointed out the importance of mass accretion in the evolution of dense cores (Padoan et al. 2014; Pelkonen et al. 2020). These different scenarios lead to different CMFs. Thus, the observed characteristics of CMFs provide a key to constraining the star formation scenarios.

Many previous studies of CMFs toward nearby star-forming regions have revealed that the CMFs resemble the IMF (e.g., Motte et al. 1998; Alves et al. 2007). For example, Alves et al. (2007) identified dense cores in the Pipe Nebula based on near-infrared extinction observations, and showed that the CMF in the Pipe Nebula has a similar slope to the IMF of the Orion Nebula Cluster (ONC) but its turnover mass is somewhat larger than that of the IMF at  $\sim 0.1 M_{\odot}$ . They suggest that if 30%–40% of the core mass goes into a star or stellar system forming inside, the turnover mass of the resultant IMF from the Pipe Nebula CMF would coincide with that of the IMF in the ONC region. However, very recently, Motte et al. (2018) reported a shallower CMF in the high-mass star-forming region, W33, and suggested the possibility of a time-evolved CMF. This evolution is further investigated in Sanhueza et al. (2019) and Kong (2019) in infrared dark clouds, considering the studies of Liu et al. (2018) and Cheng et al. (2018). The effect of a time-evolved CMFs is also discussed in detail in Clark et al. (2007) and Dib et al. (2010). It is worth noting that Kroupa & Jerabkova (2019) also discussed the variations of IMFs from region to region.

In this Letter, we compare the CMF and IMF in the ONC region, using a high-angular resolution  $C^{18}O$  ( $J = 1-0$ ) map (Kong et al. 2018). The core catalog in the whole Orion A cloud will be presented in a forthcoming paper. Our analysis presented below is the first direct comparison between the CMF and the IMF in the ONC region, in the mass range from  $10^{-1} M_{\odot}$  to  $10^2 M_{\odot}$ .

## 2. Observations and Data

### 2.1. $C^{18}O$ ( $J = 1-0$ ) Data

We use the wide-field  $C^{18}O$  ( $J = 1-0$ , 109.782182 GHz) data from the CARMA-NRO Orion survey, for which we obtained high-resolution  $^{12}CO$ ,  $^{13}CO$ , and  $C^{18}O$  maps of Orion A, by combining the data taken with the CARMA interferometer and the NRO 45 m single-dish telescope. See Kong et al. (2018) for more detail. The angular resolution of the maps is about  $8''$ , corresponding to 3300 au at a distance of 414 pc (Menten et al. 2007).<sup>28</sup> The velocity resolution is  $\sim 0.1 \text{ km s}^{-1}$ . The mean noise level of the  $C^{18}O$  map is 0.70 K ( $\approx 1\sigma$ ) in units of  $T_{\text{MB}}$ . Our map covers a  $1 \times 2$  square degree area, containing OMC-1/2/3/4, L1641N, and V380 Ori. In this Letter, we use a part of the map including the OMC-1 region and the ONC

region. The integrated intensity map of the region of interest is presented in Figure 1(a).

### 2.2. $H_2$ Column Density Data

We use the Herschel–Planck  $H_2$  column density map to calculate the core masses. The map is constructed by Kong et al. (2018) based on the  $250 \mu\text{m}$  emission map with a  $16''$  resolution and the dust temperature map with a  $36''$  resolution. We note that the angular resolution of the  $H_2$  map is twice that of our  $C^{18}O$  ( $J = 1-0$ ) map. We regridded the  $H_2$  map to match the grids of the  $C^{18}O$  ( $J = 1-0$ ) data.

### 2.3. Catalog of Young Stellar Objects (YSOs)

We use the catalog of young stars in the ONC region obtained by Da Rio et al. (2012). Their catalog includes 1619 stars whose masses and ages are derived with the DM98 model (D’Antona & Mazzitelli 1998). The spatial distribution of stars is presented in Figure 1(b). We also used the catalog of 74 Class 0 and Class I protostars in the observed region from Herschel Orion Protostar Survey (HOPS) (Furlan et al. 2016). The catalog covers the Orion A and Orion B regions with the luminosity range from  $0.06 L_{\odot}$  to  $607 L_{\odot}$ . It is worth noting that the completeness of the HOPS catalog is only about 50% (Megeath et al. 2016). Therefore, we miss a significant number of true protostellar cores. However, as shown below, the number of starless cores is much larger, and the incomplete identification of protostellar cores may not influence the shape of the CMF significantly.

Figure 2 shows the distribution of the young stars identified by Da Rio et al. (2012) as a function of age. Most of the stars have inferred ages of about  $< 2$  Myr with a tail to the age distribution out to 10 Myr (see Palla & Stahler 1999). However, as cautioned by Hartmann (2001), the various observational uncertainties can create similar age distributions even if the underlying stellar population is coeval, which makes it difficult to robustly infer the star formation rate history. The estimated star formation rate is  $\sim 1.5 \times 10^{-4} M_{\odot} \text{ yr}^{-1}$  if the stars with inferred ages less than 2 Myr are considered.

## 3. Dense Cores and CMF in the ONC Region

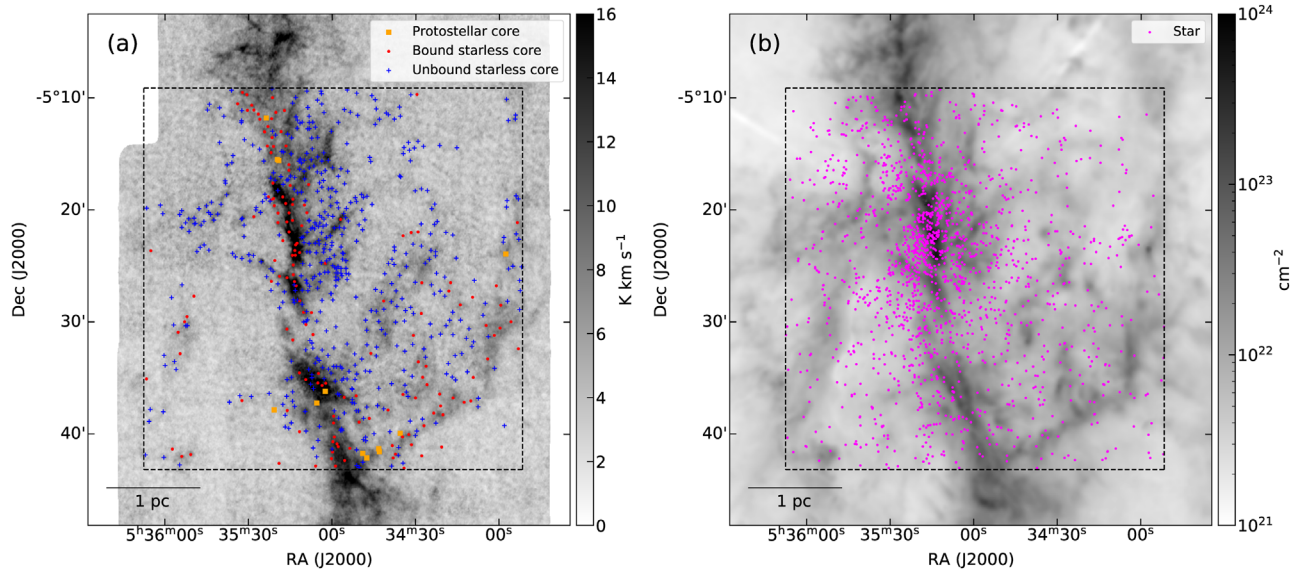
### 3.1. Core Identification

First, to verify whether our  $C^{18}O$  data can trace the dense structures reasonably well, we compare the  $C^{18}O$  column density with the  $H_2$  column density derived from dust emission. Figure 3(a) indicates the correlation between the mean  $C^{18}O$  integrated intensity and the mean  $H_2$  column density in each projected core area. The solid line indicates the optically thin LTE emission. When  $T_{\text{ex}} = 20$  K, the abundance ratio of  $C^{18}O$  with respect to  $H_2$ ,  $X_{C^{18}O}$ , is calculated as  $6.5 \times 10^{-7}$ . The  $C^{18}O$  integrated intensity is roughly proportional to the Herschel–Planck  $H_2$  column density over the range of  $\lesssim 10^{23} \text{ cm}^{-2}$ . Therefore, the  $C^{18}O$  emission is considered to be a reliable tracer of molecular hydrogen mass, and we use the  $C^{18}O$  emission to search for the dense structures in the molecular cloud. However, there may be some effects of the CO depletion particularly in cold ( $T \lesssim 20$  K), dense ( $\gtrsim 10^5 \text{ cm}^{-3}$ ) regions. In this sense, the total number of cores identified below may be somewhat underestimated.

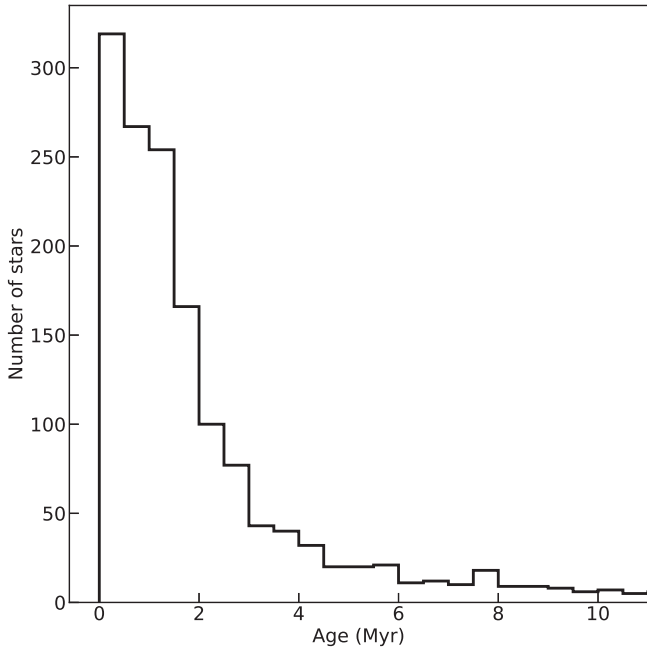
We applied astrodendro ver. 0.2.0 (Rosolowsky et al. 2008)<sup>29</sup> to the  $C^{18}O$  ( $J = 1-0$ ) data cube to identify the cores

<sup>28</sup> Based on the Gaia data, Großschedl et al. (2018) estimated the distance of 390 pc. However, we use 414 pc in this Letter. If we adopt the updated distance, the core masses tend to be about 10% smaller.

<sup>29</sup> <https://dendrograms.readthedocs.io/en/stable/>



**Figure 1.** (a) The  $\text{C}^{18}\text{O}$  integrated intensity map and (b) the Herschel–Planck  $\text{H}_2$  column density map toward the ONC region as a dashed rectangle. The identified  $\text{C}^{18}\text{O}$  cores from this study and stars in the catalog of Da Rio et al. (2012) are plotted onto (a) and (b), respectively. In (a), the squares, circles, and crosses represent the protostellar cores, gravitationally bound starless cores, and unbound starless cores, respectively.



**Figure 2.** The histogram of the stellar age in the ONC region from Da Rio et al. (2012) with the DM98 model.

by using the hierarchical structures of the molecular cloud. Here, we define a *leaf* (the smallest structure identified by *astrodendro*) as a core. Then, we estimate the masses of the cores using the Herschel–Planck  $\text{H}_2$  column density map, but we remove the contribution of the ambient gas distributed outside the cores in the position–position–velocity space.

From the CMF analysis with *clumpfind*, Pineda et al. (2009) pointed out that the CMF shapes sometimes depend on the parameters of *clumpfind*, and recommended using the core identification methods, which take into account the cloud hierarchical nature, e.g., dendrogram. Besides, recent synthetic observation studies applying dendrogram to the numerical simulation data showed that the structures identified in the PPP space are well related to the structures identified in the PPV

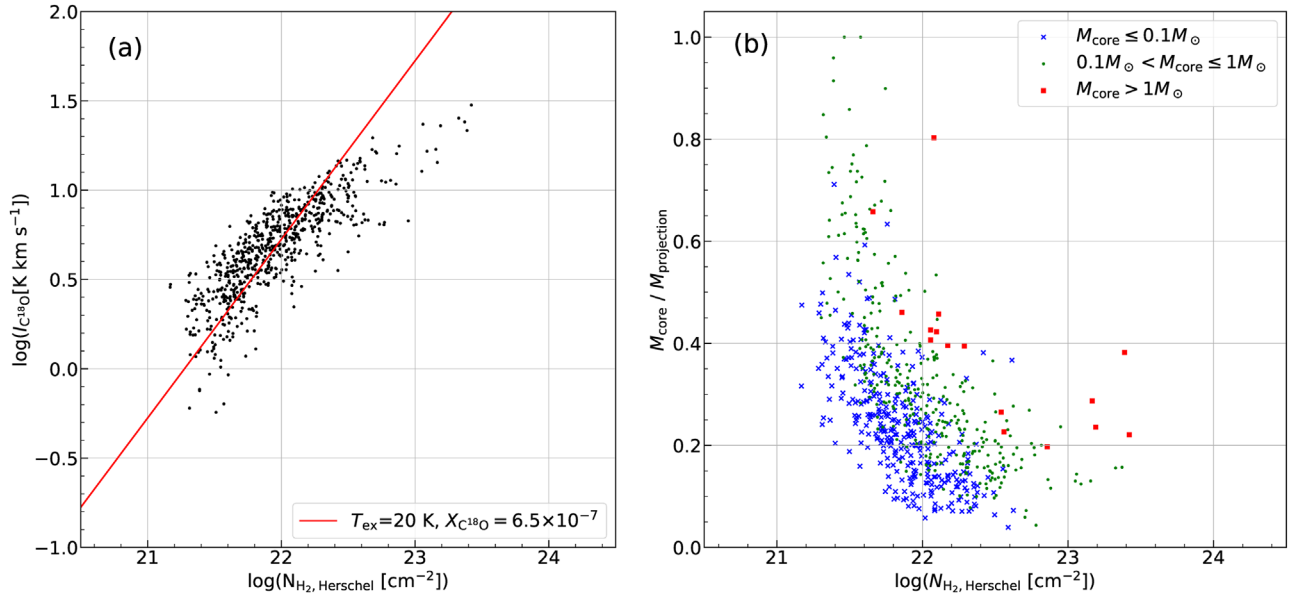
space (Beaumont et al. 2013; Burkhardt et al. 2013). Thus, we believe that our definition of dense cores is reasonable for the statistical analysis of CMFs.

In the actual identification, the three input parameters of *astrodendro* are set to  $\text{min\_delta} = 1.4 \text{ K}$  ( $\approx 2\sigma$ ),  $\text{min\_value} = 1.4 \text{ K}$  ( $\approx 2\sigma$ ), and  $\text{min\_npix} = 60$  ( $\approx 1 \text{ beam} \times 3 \text{ channels}$ ), following the suggestions of Rosolowsky et al. (2008). Additional selection criteria are imposed to minimize the effect of the spatially varying noise levels for the core identification: (1) the peak intensity of the *leaf* should be larger than  $4\sigma$  at the corresponding spatial position and (2) more than three successive channels should contain more than 20 pixels ( $\approx$  a map angular resolution) for each channel. In total, we identified 692 cores.

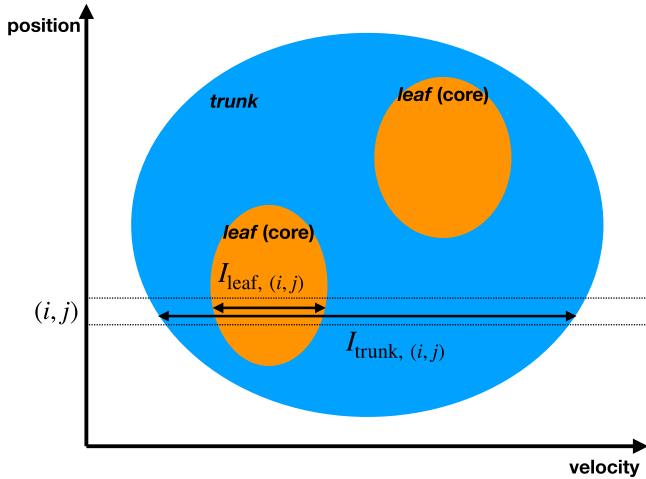
Then, we classify the cores into two groups, starless and protostellar cores, using the HOPS catalog. If a core overlaps spatially with at least one HOPS object in the sky, we classify it as a protostellar core. A core without overlapping HOPS objects is categorized as a starless core. As a result, we identified 680 starless cores and 12 protostellar cores. We note that almost all the HOPS class 0/I objects (20/21) are identified as *leaves*, but about half of such *leaves* are not satisfied with our additional condition (2). As a result, they are not classified into protostellar cores and we simply omit such cores in this Letter.

Figure 1(a) shows the spatial distribution of starless and protostellar cores in the ONC region. The cores are distributed over the entire square box in Figure 1(a). We calculated the core mass using the Herschel–Planck  $\text{H}_2$  column density ( $N_{\text{H}_2}^{\text{Herschel}}$ ) and intensity-ratio of the *leaf* and the *trunk* ( $I_{\text{leaf}}/I_{\text{trunk}}$ ) (see Figure 4). We assigned the  $\text{H}_2$  column density to each core using the intensity-ratio and calculated the core mass as  $M_{\text{core}} = 3 \times 10^{-3} \times \sum(N_{\text{H}_2}^{\text{Herschel}}(i, j)/10^{22} \text{ cm}^{-2}) \times I_{\text{leaf}}(i, j)/I_{\text{trunk}}(i, j)$ , where  $i$  and  $j$  are the indices of the cell of interest on the R.A.–decl. plane, respectively. Figure 3(b) shows the mass ratio of  $M_{\text{core}}$ , core mass, and  $M_{\text{projection}}$ . The mass  $M_{\text{projection}}$  is calculated by integrating all  $\text{H}_2$  column density contained within the projection of cores (i.e.,  $M_{\text{projection}} = 3 \times 10^{-3} \times \sum(N_{\text{H}_2}^{\text{Herschel}}(i, j)/10^{22} \text{ cm}^{-2})$ ). The mean mass ratio is  $\sim 0.29$ .





**Figure 3.** (a) The correlation between the mean  $C^{18}O$  ( $J = 1-0$ ) integrated intensity and the mean Herschel–Planck  $H_2$  column density in each projected core area. The solid line shows the best-fit function of optically thin LTE emission which is based on an abundance ratio of  $X_{C^{18}O} = 6.5 \times 10^{-7}$  when  $T_{\text{ex}} = 20$  K. (b) The relationship between the mass ratio,  $M_{\text{core}}/M_{\text{projection}}$  and the Herschel–Planck  $H_2$  column density.



**Figure 4.** Cartoon of dendrogram’s hierarchical structures of intensity focusing on a *trunk* and a *leaf* in the position–velocity plane. The two arrows represent the intensity of a *trunk* and a *leaf*.

Using a virial analysis, we classify the starless cores into gravitationally bound cores and unbound cores with the threshold of  $\alpha_{\text{vir}} = M_{\text{vir}}/M_{\text{core}} = 2$  and also show their distribution in Figure 1(a). For the virial mass  $M_{\text{vir}}$ , we assumed a centrally condensed sphere without magnetic fields and external pressure as  $M_{\text{vir}} = 126(R_{\text{core}}/\text{pc})(dV_{\text{core}}/\text{km s}^{-1})^2$ .

We calculated the core radius  $R_{\text{core}}$  using a projected area of a core onto the plane of the sky,  $A_{\text{core}}$ , as  $R_{\text{core}} = \sqrt{A_{\text{core}}/\pi}$ . Here, the area,  $A_{\text{core}}$ , and velocity dispersion,  $v_{\text{rms}}$  which is the intensity-weighted second moment of velocity, are calculated by *astrodendro*. We categorized 151 starless cores,  $\sim 22\%$  of starless cores, as gravitationally bound starless cores. We also calculated the core density as  $\rho_{\text{core}}$  as  $\rho_{\text{core}} = M_{\text{core}}/(4/3)\pi R_{\text{core}}^3$ . The mean values and standard deviations of diameters, velocity widths in FWHM, masses, densities, and virial ratios of the starless cores are  $0.065 \pm 0.022$  pc,  $0.34 \pm 0.13$  km  $s^{-1}$ ,  $0.19 \pm 0.42 M_{\odot}$ ,  $(2.4 \pm 4.6) \times 10^4$   $\text{cm}^{-3}$ , and  $4.8 \pm 4.1$ , respectively.

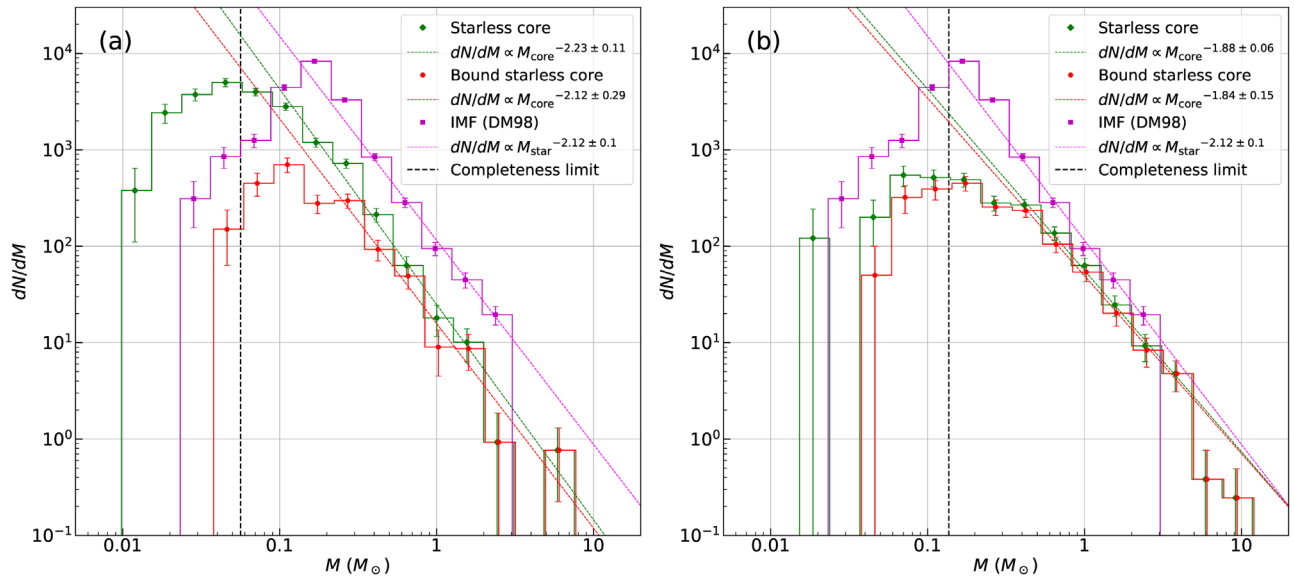
#### 4. CMFs in the ONC Region

Figure 5(a) shows the CMFs toward ONC for all the starless cores and self-gravitating starless cores. For comparison, we show the stellar IMF in Figure 5. The shapes of the CMFs are similar to those of the stellar IMF. All CMFs have best-fit power-law indices of  $\sim -2$  at the high-mass end. The CMFs for all starless cores and self-gravitating cores have the turnover masses of  $\sim 0.05 M_{\odot}$  (below the completeness limit) and  $\sim 0.11 M_{\odot}$ , respectively, which are comparable to that of the IMF.

The results of the core identification depend on the adopted parameters of *astrodendro*. When we set  $\text{min\_delta} = 3\sigma$ ,  $\text{min\_value} = 3\sigma$ , and  $\text{min\_npix} = 120$  as the *astrodendro* parameters, we identified 270 starless cores and 224 bound starless cores. For comparison, we show the CMF derived with the above parameters in Figure 5(b). The turnover masses of CMFs for starless cores and bound starless cores are  $\sim 0.07 M_{\odot}$  and  $\sim 0.17 M_{\odot}$ , respectively. The differences in turnover masses of each CMF for different parameters are within 1 mass bin. Thus, we conclude that the dendrogram’s parameters do not change the turnover mass dramatically.

We calculated completeness by inserting into the map artificial cores that have a size corresponding to the beam size and FWHM line width of three channels ( $0.3$  km  $s^{-1}$ ). The total fluxes are calculated by assuming optically thin emission of  $C^{18}O$  ( $J = 1-0$ ) with  $T_{\text{ex}}$  and  $X_{C^{18}O}$  derived in Figure 3(a) and a central mass of each mass bin. We inserted one core to the data, of which the position is random in trunks with avoiding the center overlaps observed cores. Then, we applied *astrodendro* to check if it is identified as a *leaf*. By repeating the procedure 1000 times for each mass bin, we calculated the detection probability. The 90% completeness limits are shown as vertical dashed lines in Figure 5.

Ikeda & Kitamura (2009) derived the CMF in almost the same region using the same line  $C^{18}O$  ( $J = 1-0$ ). They derived the turnover mass at  $\sim 5 M_{\odot}$ , about 20 times larger than our value. They suggested that their turnover mass is an artifact of



**Figure 5.** CMFs in the ONC region. The astrodendro’s parameters are (a)  $\text{min\_delta} = 2\sigma$ ,  $\text{min\_value} = 2\sigma$ , and  $\text{min\_npix} = 60$  and (b)  $\text{min\_delta} = 3\sigma$ ,  $\text{min\_value} = 3\sigma$ , and  $\text{min\_npix} = 120$ , respectively. For comparison, we show the IMF derived by Da Rio et al. (2012) in both panels. The 90% completeness limit is indicated with the vertical dashed lines. The error bars denote statistical errors.

the poor angular resolution. The effect of angular resolution on the turnover mass is also discussed in Reid et al. (2010). There are two main differences between Ikeda & Kitamura’s (2009) and our analyses. One is the core identification method adopted. Ikeda & Kitamura (2009) used clumpfind algorithm (Williams et al. 1994) which tends to define a core as a structure larger than that identified with dendrogram since clumpfind algorithm allocates all pixels above a threshold to one of the cores. The more important difference is the angular resolution. In fact, applying the dendrogram to the NRO 45 m only data with  $26''$  resolution, Takemura et al. (2020) derived the turnover mass of about  $0.5 M_{\odot}$ . This is about 5 times larger than that derived in this study. If the turnover mass depends only on the angular resolution, the artificial turnover mass obtained from the CARMA-NRO data is about  $0.5/(26/8)^2 M_{\odot} \sim 0.05 M_{\odot}$ . On the other hand, our obtained turnover mass for the bound cores is about  $0.1 M_{\odot}$ , larger than the value expected from the difference of the angular resolution ( $0.05 M_{\odot}$ ). Thus, we believe that we constrain the true turnover mass for the bound cores reasonably well.

## 5. Discussion

The IMF in the ONC region is reproduced from our derived CMFs if it is assumed that (1) the star formation efficiency (SFE) of individual cores is constant over the whole mass range as discussed by Alves et al. (2007) and (2) the SFE of individual cores is 100%. However, assuming an SFE of 100% is unphysical, because mass-loss through a protostellar jet is a necessary part of the accretion process, with theoretical models, simulations and observations suggesting that  $\sim 30\%$  of the accreting mass is lost that way (see the review by Pudritz et al. 2007). Furthermore, the feedback from outflows can also disperse part of the core mass, with the combined effect of jets and outflow feedback leading to an SFE of order 30% (e.g., Federrath et al. 2014). Thus, our results suggest that mass accretion onto the cores from a larger reservoir must be an ongoing process.

According to the standard scenario of star formation, the prestellar cores must be self-gravitating to initiate star formation. Assuming that all the self-gravitating starless cores ( $\alpha_{\text{vir}} < 2$ ) form stars within a few freefall times, we can evaluate the future star formation rate in this region. Assuming that the star formation timescale is about three times the freefall time with the mean density of bound starless cores of  $4 \times 10^4 \text{ cm}^{-3}$ , the future star formation rate is calculated to be  $1 \times 10^{-4} M_{\odot} \text{ yr}^{-1}$ . This is almost comparable to the recent star formation rate obtained in Section 2.3. Thus, our results seem to suggest that self-gravitating cores are likely to be direct progenitors of stars in the ONC region. However, we cannot rule out the possibility of star formation from the gravitationally unbound cores since the star formation rate would be only doubled even if all the starless cores form stars within a few freefall time. Recent studies suggest that the majority of the cores are unbound (Maruta et al. 2010; Kirk et al. 2017), and such cores become gravitationally bound or disperse eventually (Chen et al. 2020; Smullen et al. 2020).

If the accretion plays a role in determining the final stellar mass, we expect that our identified protostellar core population has a larger mean mass compared to that of the starless cores. The mean masses of starless cores and protostellar cores are  $\sim 0.19 M_{\odot}$  and  $\sim 0.67 M_{\odot}$ , respectively. For protostellar core masses, we do not include the masses of protostars located inside. This larger mean mass for the protostellar cores is consistent with the idea that the starless cores gain significant gas from the surroundings during star formation. The importance of the mass accretion onto the cores is also pointed out by Dib et al. (2010).

## 6. Conclusions

In this Letter we have compared for the first time the CMF and IMF in the same region, which is located in the ONC. Determinations of the two functions with comparable sensitivities have revealed that the CMF has a turnover mass of  $\sim 0.1 M_{\odot}$ , which is comparable to that of the IMF (see also Bontemps et al. 2001, for  $\rho$  Oph). This seems to contradict the

previous conclusion of a larger turnover mass of CMFs (e.g., Nutter & Ward-Thompson 2007; Anathpindika 2011). This difference may simply come from the difference in the angular resolutions of the observations.

To keep the slope of the CMF unchanged over time (so that the resultant IMF resembles the stellar IMF observed), the mass accretion rate onto individual cores should be proportional to  $M_{\text{core}}$  if the timescale of the accretion is more or less constant. The importance of the mass accretion appears to favor the competitive accretion scenario. However, according to the Bondi–Hoyle–Littleton accretion scenario the mass accretion rate is proportional to  $M_{\text{core}}^2$ , and thus, the slopes of the CMFs can change with time (e.g., Goodwin et al. 2008). Numerical simulations also indicate that the actual accretion rates are significantly influenced by environments such as the global gravitational potential, and vary with time (e.g., Klessen 2001; Girichidis et al. 2012). Our result indicates that the mass functions of the stellar seeds already resemble the IMF if the stellar seeds form by the gravitational collapse of the identified prestellar cores. Recent numerical simulations have pointed out the importance of mass accretion in the evolution of dense cores (Padoan et al. 2014; Haugbølle & Padoan 2018), leading to the inertial-inflow scenario. In contrast to both the core-collapse and the competitive accretion models, the inertial-inflow model stresses the role of inertial turbulent flows in assembling the stellar mass from a large-scale mass reservoir (Padoan et al. 2020), even if the CMF and the IMF are very similar (Pelkonen et al. 2020), as found in this work.

Recent observations have detected the infall motions toward the prestellar cores (Contreras et al. 2018). A significant amount of parent core mass is likely to be blown out by the stellar feedback (e.g., Machida & Matsumoto 2012). If the stellar feedback is important in determining the core mass, prestellar cores need to gain much more mass from the surroundings (Sanhueza et al. 2019).

Data analysis was carried out on the Multi-wavelength Data Analysis System operated by the Astronomy Data Center (ADC), National Astronomical Observatory of Japan. Part of this research was carried out at the Jet Propulsion Laboratory, California Institute of Technology, under a contract with the National Aeronautics and Space Administration. P.S. was partially supported by a Grant-in-Aid for Scientific Research (KAKENHI Number 18H01259) of Japan Society for the Promotion of Science (JSPS). R.S.K. acknowledges financial support from the DFG via the collaborative research center (SFB 881, Project-ID 138713538) “The Milky Way System” (subprojects A1, B1, B2, and B8). He is also thankful for subsidies from the Heidelberg Cluster of Excellence *STRUCTURES* in the framework of Germany’s Excellence Strategy (grant EXC-2181/1-390900948) and for funding from the European Research Council (ERC) via the ERC Synergy Grant *ECOGAL* (grant 855130). P.P. acknowledges support by the Spanish MINECO under project AYA2017-88754-P, and financial support from the State Agency for Research of the Spanish Ministry of Science and Innovation through the “Unit of Excellence María de Maeztu 2020-2023” award to the Institute of Cosmos Sciences (CEX2019-000918-M). V.O., A.S.M., and P.S. were supported by the Collaborative Research Centre 956, subprojects C1, A6, and C3, funded by the Deutsche Forschungsgemeinschaft (DFG), project ID 184018867. T.G.S.P. gratefully acknowledges support by the National Science Foundation under grant No. AST-2009842. J.E.P. acknowledges

the support by the Max Planck Society. We thank the anonymous referee for many useful comments that have improved the presentation.

*Facilities:* CARMA, No:45 m, Herschel.

*Software:* The data analysis in this paper uses python packages Astropy (Astropy Collaboration et al. 2013), SciPy (Virtanen et al. 2020), Numpy (van der Walt et al. 2011), APLpy, Matplotlib (Hunter 2007) and Astrodendro (Rosolowsky et al. 2008).

## ORCID iDs

Hideaki Takemura  <https://orcid.org/0000-0003-2902-2038>  
 Fumitaka Nakamura  <https://orcid.org/0000-0001-5431-2294>  
 Shuo Kong  <https://orcid.org/0000-0002-8469-2029>  
 Héctor G. Arce  <https://orcid.org/0000-0001-5653-7817>  
 John M. Carpenter  <https://orcid.org/0000-0003-2251-0602>  
 Volker Ossenkopf-Okada  <https://orcid.org/0000-0002-8351-3877>  
 Ralf Klessen  <https://orcid.org/0000-0002-0560-3172>  
 Patricio Sanhueza  <https://orcid.org/0000-0002-7125-7685>  
 Yoshito Shimajiri  <https://orcid.org/0000-0001-9368-3143>  
 Takashi Tsukagoshi  <https://orcid.org/0000-0002-6034-2892>  
 Ryohei Kawabe  <https://orcid.org/0000-0002-8049-7525>  
 Shun Ishii  <https://orcid.org/0000-0001-8337-4961>  
 Kazuhito Dobashi  <https://orcid.org/0000-0001-8058-8577>  
 Tomomi Shimoikura  <https://orcid.org/0000-0002-1054-3004>  
 Paul F. Goldsmith  <https://orcid.org/0000-0002-6622-8396>  
 Álvaro Sánchez-Monge  <https://orcid.org/0000-0002-3078-9482>  
 Jens Kauffmann  <https://orcid.org/0000-0002-5094-6393>  
 Thushara G. S. Pillai  <https://orcid.org/0000-0003-2133-4862>  
 Paolo Padoan  <https://orcid.org/0000-0002-5055-5800>  
 Adam Ginsberg  <https://orcid.org/0000-0001-6431-9633>  
 Rowan J. Smith  <https://orcid.org/0000-0002-0820-1814>  
 John Bally  <https://orcid.org/0000-0001-8135-6612>  
 Steve Mairs  <https://orcid.org/0000-0002-6956-0730>  
 Jaime E. Pineda  <https://orcid.org/0000-0002-3972-1978>  
 Dariusz C. Lis  <https://orcid.org/0000-0002-0500-4700>  
 Blakesley Burkhart  <https://orcid.org/0000-0001-5817-5944>  
 Peter Schilke  <https://orcid.org/0000-0003-2141-5689>  
 Hope How-Huan Chen  <https://orcid.org/0000-0001-6222-1712>  
 Andrea Isella  <https://orcid.org/0000-0001-8061-2207>  
 Alyssa A. Goodman  <https://orcid.org/0000-0003-1312-0477>

## References

- Alves, J., Lombardi, M., & Lada, C. J. 2007, *A&A*, 462, L17  
 Anathpindika, S. 2011, *NewA*, 16, 477  
 Astropy Collaboration, Robitaille, T. P., Tollerud, E. J., et al. 2013, *A&A*, 558, A33  
 Ballesteros-Paredes, J., André, P., Hennebelle, P., et al. 2020, *SSRv*, 216, 76  
 Beaumont, C. N., Offner, S. S. R., Shetty, R., Glover, S. C. O., & Goodman, A. A. 2013, *ApJ*, 777, 173  
 Bonnell, I. A., & Bate, M. R. 2006, *MNRAS*, 370, 488  
 Bontemps, S., André, P., Kaas, A. A., et al. 2001, *A&A*, 372, 173  
 Burkhart, B., Lazarian, A., Goodman, A., & Rosolowsky, E. 2013, *ApJ*, 770, 141  
 Chen, H. H.-H., Offner, S. S. R., Pineda, J. E., et al. 2020, arXiv:2006.07325

- Cheng, Y., Tan, J. C., Liu, M., et al. 2018, *ApJ*, **853**, 160
- Clark, P. C., Klessen, R. S., & Bonnell, I. A. 2007, *MNRAS*, **379**, 57
- Contreras, Y., Sanhueza, P., Jackson, J. M., et al. 2018, *ApJ*, **861**, 14
- Da Rio, N., Robberto, M., Hillenbrand, L. A., Henning, T., & Stassun, K. G. 2012, *ApJ*, **748**, 14
- D'Antona, F., & Mazzitelli, I. 1998, in ASP Conf. Ser. 134, Brown Dwarfs and Extrasolar Planets, ed. R. Rebolo, E. L. Martin, & M. R. Zapatero Osorio (San Francisco, CA: ASP), 442
- Dib, S., Shadmehri, M., Padoan, P., et al. 2010, *MNRAS*, **405**, 401
- Federrath, C., Schrön, M., Banerjee, R., & Klessen, R. S. 2014, *ApJ*, **790**, 128
- Furlan, E., Fischer, W. J., Ali, B., et al. 2016, *ApJS*, **224**, 5
- Girichidis, P., Federrath, C., Banerjee, R., & Klessen, R. S. 2012, *MNRAS*, **420**, 613
- Goodwin, S. P., Nutter, D., Kroupa, P., Ward-Thompson, D., & Whitworth, A. P. 2008, *A&A*, **477**, 823
- Großschedl, J. E., Alves, J., Meingast, S., et al. 2018, *A&A*, **619**, A106
- Hartmann, L. 2001, *AJ*, **121**, 1030
- Haugbølle, T., Padoan, P., & Nordlund, Å. 2018, *ApJ*, **854**, 35
- Hunter, J. D. 2007, *CSE*, **9**, 90
- Ikeda, N., & Kitamura, Y. 2009, *ApJL*, **705**, L95
- Kirk, H., Friesen, R. K., Pineda, J. E., et al. 2017, *ApJ*, **846**, 144
- Klessen, R. S. 2001, *ApJL*, **550**, L77
- Klessen, R. S., Burkert, A., & Bate, M. R. 1998, *ApJL*, **501**, L205
- Klessen, R. S., & Hennebelle, P. 2010, *A&A*, **520**, A17
- Kong, S. 2019, *ApJ*, **873**, 31
- Kong, S., Arce, H. G., Feddersen, J. R., et al. 2018, *ApJS*, **236**, 25
- Kroupa, P., & Jerabkova, T. 2019, *NatAs*, **3**, 482
- Liu, M., Tan, J. C., Cheng, Y., & Kong, S. 2018, *ApJ*, **862**, 105
- Machida, M. N., & Matsumoto, T. 2012, *MNRAS*, **421**, 588
- Maruta, H., Nakamura, F., Nishi, R., Ikeda, N., & Kitamura, Y. 2010, *ApJ*, **714**, 680
- McKee, C. F., & Tan, J. C. 2003, *ApJ*, **585**, 850
- Megeath, S. T., Gutermuth, R., Muzerolle, J., et al. 2016, *AJ*, **151**, 5
- Menten, K. M., Reid, M. J., Forbrich, J., & Brunthaler, A. 2007, *A&A*, **474**, 515
- Motte, F., Andre, P., & Neri, R. 1998, *A&A*, **336**, 150
- Motte, F., Nony, T., Louvet, F., et al. 2018, *NatAs*, **2**, 478
- Nutter, D., & Ward-Thompson, D. 2007, *MNRAS*, **374**, 1413
- Padoan, P., Haugbølle, T., & Nordlund, Å. 2014, *ApJ*, **797**, 32
- Padoan, P., Pan, L., Juvela, M., Haugbølle, T., & Nordlund, Å. 2020, *ApJ*, **900**, 82
- Palla, F., & Stahler, S. W. 1999, *ApJ*, **525**, 772
- Pelkonen, V. M., Padoan, P., Haugbølle, T., & Nordlund, Å. 2020, arXiv:2008.02192
- Pineda, J. E., Rosolowsky, E. W., & Goodman, A. A. 2009, *ApJL*, **699**, L134
- Pudritz, R. E., Ouyed, R., Fendt, C., & Brandenburg, A. 2007, in Protostars and Planets V, ed. B. Reipurth, D. Jewitt, & K. Keil (Tucson, AZ: Univ. Arizona Press), 277
- Reid, M. A., Wadsley, J., Petitclerc, N., & Sills, A. 2010, *ApJ*, **719**, 561
- Rosolowsky, E. W., Pineda, J. E., Kauffmann, J., & Goodman, A. A. 2008, *ApJ*, **679**, 1338
- Sanhueza, P., Contreras, Y., Wu, B., et al. 2019, *ApJ*, **886**, 102
- Shu, F. H., Adams, F. C., & Lizano, S. 1987, *ARA&A*, **25**, 23
- Smullen, R. A., Kratter, K. M., Offner, S. S. R., Lee, A. T., & Chen, H. H.-H. 2020, *MNRAS*, **497**, 4517
- Takemura, H., Nakamura, F., Ishii, S., et al. 2020, PASJ, in press (arXiv:2103.08526)
- van der Walt, S., Colbert, S. C., & Varoquaux, G. 2011, *CSE*, **13**, 22
- Vázquez-Semadeni, E., Palau, A., Ballesteros-Paredes, J., Gómez, G. C., & Zamora-Avilés, M. 2019, *MNRAS*, **490**, 3061
- Virtanen, P., Gommers, R., Oliphant, T. E., et al. 2020, *NatMe*, **17**, 261
- Wang, P., Li, Z.-Y., Abel, T., & Nakamura, F. 2010, *ApJ*, **709**, 27
- Williams, J. P., de Geus, E. J., & Blitz, L. 1994, *ApJ*, **428**, 693
- Zinnecker, H. 1982, *NYASA*, **395**, 226